The VIVACE Converter: Model Tests at High Damping and Reynolds Number Around 10^5

Michael M. Bernitsas
Ph.D. Professor
Fellow ASME

Y. Ben-Simon
Graduate Student
N.A. Professional Degree

Kamaldev Raghavan
Graduate Student
Ph.D Candidate

E. M. H. Garcia
Graduate Student
Ph.D Candidate

Department of Naval Architecture and Marine Engineering,
University of Michigan,
2600 Draper Road,
Ann Arbor, MI 48109-2145

The vortex induced vibrations for aquatic clean energy (VIVACE) converter is a new concept to generate clean and renewable energy from fluid flows such as those abundant in oceans, rivers, or other water resources. The underlying concepts for design, scaling, and operation of VIVACE were introduced in Bernitsas et al., 2008, "VIVACE (Vortex Induced Vibration Aquatic Clean Energy): A New Concept in Generation of Clean and Renewable Energy From Fluid Flow," ASME J. Offshore Mech. Arct. Eng., ***130****(4), p. 041101. In its simplest form, a VIVACE modulo consists of a single rigid cylinder mounted on elastic supports and connected to a power takeoff (PTO) system. The cylinder is placed in a steady unidirectional current and excited in vortex induced vibration (VIV). In this paper, the VIVACE modulo was tested in the Low Turbulence Free-Surface Water Channel of the University of Michigan to demonstrate the concept, generate electricity, measure the power out, and calculate basic benchmarking measures such as energy density. The tests performed were tailored to the particulars of the VIVACE modulo, which dictate that the cylinder operate in VIV under high damping and as high a Reynolds number as possible. At the same time, a broad range of synchronization is required to make VIVACE effective in energy generation in a realistic environment. Due to these requirements, VIV tests have not been performed before in the subspace applicable to the operation of the VIVACE modulo. In the process of extracting fluid kinetic energy and converting it to electricity in the laboratory, for a given set of cylinder-springs-transmission-generator, only the damping used for harnessing electricity was optimized. Even at this early stage of development, for the tested VIVACE modulo, the maximum peak power achieved was* $P_{peak}=0.308\times\frac{1}{2}\rho DLL$. *The corresponding integrated power in that particular test was* $P_{VIVACE}=0.22\times\frac{1}{2}\rho U^3DL$ *with theoretical upper limit based on measurements of* $P_{UL-VIVACE}=0.3663$. *Such power was achieved at velocity* $U=0.840\ m/s=1.63\ Kn$. [DOI: 10.1115/1.2979796]

1 Problem Definition

Generation of energy by a VIVACE converter is based on extracting kinetic energy from a fluid flow by exciting a rigid cylinder on elastic supports in VIV. A brief literature review on VIV, ocean energy conversion, and VIVACE was presented in Ref. [1]. Suffice to discuss here only some important issues directly relating to the domain of operation of VIVACE so the relevant problem can be defined.

1.1 Literature Review. There are five sources of energy in the ocean: waves, tides, currents, thermal gradient, and saline gradient [2]. Numerous devices have been designed and or built to generate energy from those resources [3]. Most devices that extract kinetic energy from the ocean use oscillating buoys, water columns, or flaps in waves, and water mills or turbines in currents. The VIVACE Converter appears to be unique in its underlying principle of extracting energy from water flows [1,4–7]. VIV for energy extraction appears in one previous patent [8], which obviously cannot work because it suppresses VIV in a multitude of ways. Also, in Ref. [9], a miniscule amount of energy is extracted as a byproduct of damping the VIV of towers.

VIV has been studied extensively since 1504 A.D. when it was first observed by Leonardo da Vinci in the form of Aeolian tones. Most experimental and analytical works have been done since the early 1900s. Great progress in our understanding of VIV has been achieved in the last decade. Typically, VIV studies focus on the low-Reynolds number regime and for low damping. The first applications of the VIVACE on which we are working operate in the high Reynolds and high damping regime where very little experimental work is available. The reason is that VIV is a very complex nonlinear, self-limiting, self-induced, multidegree-of-freedom phenomenon, which is affected by many parameters and exhibits several different modes of responses. The difficulties experienced in understanding and describing the nature of VIV, its dependence on parameters and predicting its response, have been reviewed in Refs. [10–30].

There are several issues in VIV that affect the design and operation of the VIVACE converter. Those were presented in Ref. [1] and are the following.

(a) *Synchronization or lock-in between vortex shedding and cylinder oscillation* [16,18]. As the flow velocity U increases, lock-in for a high mass ratio system is reached when the vortex formation frequency $f_{V,\text{form}}$ is close enough to the body's natural frequency $f_{n,\text{water}}$. The two frequencies involved, $f_{V,\text{form}}$ and $f_{n,\text{water}}$, may be far apart depending on the mass ratio m^*. This also affects the wake pattern mode.

(b) *Range of synchronization* [16–18]. Unlike linear systems, which achieve a large amplitude response in a narrow band around their natural frequency, systems in VIV achieve large amplitudes over broad ranges around $f_{n,\text{water}}$. This is a major advantage for a VIVACE con-

Contributed by the Ocean Offshore and Arctic Engineering Division of ASME for publication in the JOURNAL OF OFFSHORE MECHANICS AND ARCTIC ENGINEERING. Manuscript received July 3, 2006; final manuscript received December 26, 2007; published online December 11, 2008. Assoc. Editor: Dan Valentine. Paper presented at the 25th International Conference on Offshore Mechanics and Arctic Engineering (OMAE2006), Hamburg, Germany, June 4–9, 2006.

verter as it results in robustness as far as sensitivity to relatively large changes in flow velocity.

(c) *Self-limiting amplitude* [16–18]. On the other hand, the amplitude of oscillation of a cylinder in VIV is self-limiting as large motions break the wake mode and vortex pattern. This is not restrictive to the design concept of a VIVACE converter as we introduce energy harnessing resistance R_L enough to maintain the large amplitude oscillation but not big enough to suppress VIV.

(d) *Amplitude of oscillation and associated branches: initial, upper, and lower*. Over the synchronization regime, these three branches correspond to different amplitudes and wake patterns [18]. It is important for VIVACE to operate under high damping and sustain high amplitude oscillations (upper branch) over very wide ranges of synchronization.

(e) *Wake patterns defined as 2S, 2P, P+S, 2T* [1,18–22]. Manifestation of wake patterns is determined by m^* and a second degree-of-freedom ζ.

(f) *Ratio of oscillating mass to displaced fluid mass* m^* [18,23]. Govardhan and Williamson observed [24–26] that there exist two distinct types of response, depending on high or low combined mass-damping $m^*\zeta$. In the classical high $m^*\zeta$ case, the "initial" and "lower" amplitude branches are separated by a discontinuous mode transition; whereas in the case of low $m^*\zeta$, the upper branch appears. For large mass ratios $m^*=O(100)$ [18,46], the vibration frequency for synchronization lies close to the natural frequency $f^*_{V,\text{form}}=f_{V,\text{form}}/f_{n,\text{water}}\approx 1$. As the mass ratio is reduced to $m^*=O(1)$, $f^*_{V,\text{form}}$ can reach high values. They also derived the following expression for the vortex formation frequency in the lower branch of vibration $f_{\text{lower}}=\sqrt{(m^*+C_A)/m^*-0.54}$, where C_A is the potential flow added mass taken as one for a circular cylinder. It reveals the existence of a critical mass ratio $m^*_{\text{critic}}=0.54$, where $f^*_{V,\text{form}}$ becomes very large. When $m^*<m^*_{\text{critic}}$, the lower branch ceases to exist.

(g) *Multiple degrees-of-freedom* [18]. It has also been observed experimentally that a two degree-of-freedom cylinder in VIV allows larger amplitudes of oscillation in the direction perpendicular to the fluid flow.

(h) *Correlation length* [38]. This is an order of magnitude higher than the correlation length of a stationary cylinder in current. The larger it is, the higher are the forces exerted on the VIVACE cylinder as a whole.

(i) *Synchronization under high damping* [1]. This has received no attention up to date, and it is the regime applicable to the VIVACE converter. The higher the damping imposed by the energy harnessing resistance R_L, the more energy can be extracted provided that VIV can be maintained. This is shown in the mathematical model in Chap. I and the model test data in Chap. V.

(j) *Increase in lift with Reynolds number* [27]. To the authors' knowledge, the experiments on the VIV of cylinders at high Reynolds number are scarce [28–30]. However, recent work has shown that the amplitude of oscillation increases for high Reynolds numbers [1,28].

(k) *Proximity to free-surface or solid boundaries* [1,22,31,32,37]. The free- surface effect on the VIV of cylinders is important because when the flow is bounded by a surface the structure of the wake and the forces on the cylinder can be significantly altered, as shown in Refs. [33,34]. The boundary conditions at a free-surface are significantly different from those at a solid boundary [35,36]. This is investigated in Chap. 2 as part of the calibration process since the low turbulence free-surface water (LTFSW) channel in which the VIVACE models have been tested has a limited depth.

1.2 Problem Definition. The previous discussion on the important VIV issues and what is relevant to the VIVACE converter sets the stage for defining the problems that we need to study. Specifically, we need to conduct VIV tests for the VIVACE modulo under the following conditions:

(i) high damping so we can harness fluid kinetic energy and convert it to electricity
(ii) high Reynolds number for two reasons: first, it represents realistic conditions for the operation of this converter; and second, it increases lift forces and VIV amplitude and synchronization range
(iii) variable electrical load resistance R_L in order to optimize the harnessed energy.

Accordingly, in Chap. 2, the LTFSW channel chosen for the experiments—VIVACE Model III—and the calibration process are described. A mathematical model for the coupled VIV-transmission-generator-harnessed electricity is developed in Chap. 3 and is compatible to the hydrodynamic model developed in our previous paper [1]. In Chap. 4, the model test measurements are described and the Hilbert–Huang transform is considered for data analysis. In Chap. 5, the test results are presented showing the optimal energy extraction for a given design of the converter; the mathematical model is used to verify consistency of measurements. Conclusions and future steps in model tests and the development of the VIVACE converter are presented at the end.

2 Facility, Apparatus, and Calibration

All model tests performed on the simple VIVACE modulo considered in this paper were conducted in the LTFSW channel of the Marine Renewable Energy Laboratory (MRE Lab) of the University of Michigan. The LTFSW channel is described in Sec. 2.1 along with the reasons of selecting that facility for the VIVACE model tests. The particulars of the physical model, which was built and tested, are presented in Sec. 2.2. The calibration of the LTFSW channel with the VIVACE modulo in place is discussed in Sec. 2.3.

2.1 Low Turbulence Free-Surface Water Channel. A continuous flow past a VIVACE cylinder can be provided in the LTFSW channel. Alternatively, the current effect can be created by towing the cylinder at a constant speed in calm water. The relative flow past the cylinder is equivalent. Each method, however, has particular benefits and limitations. Careful use of a towing tank with sufficient time between runs reduces the free-stream turbulence to negligible levels but the length of the towing tank limits the number of oscillations per experiment. In the LTFSW channel, the flow is generated by an impeller, and there is no limit on the number of oscillations per experiment, but it is difficult to achieve low turbulence levels because of the turbulence induced by the impeller and the cylinder in the VIV. The length of the cylinder is limited by the width of the channel. The LTFSW channel was selected because of its advantages and acceptable turbulence level.

The purpose of the LTFSW channel is to facilitate the study of the fundamental structural aspects of turbulent flows. The water channel is two stories high and recirculates approximately 8000 gal of softened and filtered water by making use of a 0.787 m diameter four bladed bronze impeller connected to a 20 hp three-phase induction motor. The maximum flow speed is 2 m/s. The test section is 2.44 m long, 1 m across, and 0.8 m deep. All walls at the test section are acrylic to allow for flow visualization experiments and to facilitate measurements with optical instrumentation. The turbulence intensity normalized by the freestream velocity was reported at 0.095% [38].

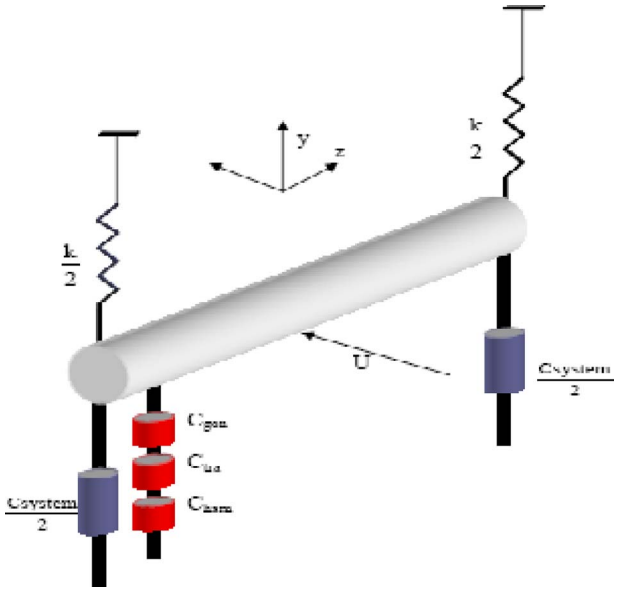

Fig. 1 Simple schematic of a VIVACE modulo with coordinate system

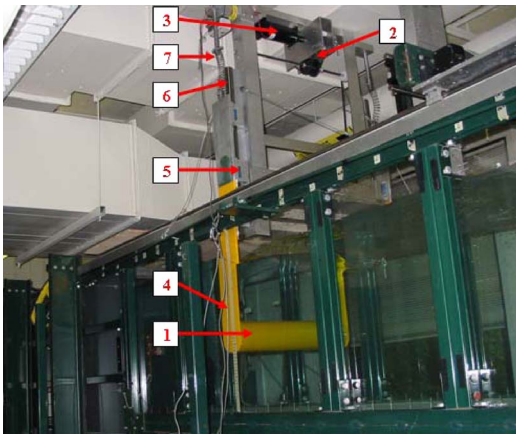

Fig. 2 VIVACE Model III in the low turbulence free-surface water channel

2.2 Apparatus. A simple schematic of a single modulo of the VIVACE converter considered in this paper is depicted in Fig. 1. Per the description in Sec. 3.1, the elements of this modulo are a circular rigid cylinder of diameter D and length L, two supporting linear springs each of stiffness $k/2$, system damping c_{system}, transmission mechanism damping c_{tra}, a generator with damping c_{gen}, and the energy harnessing damping c_{harn}. The cylinder is placed with its axis in the z-direction perpendicular to the flow velocity U, which is in the x-direction. The cylinder oscillates in the y-direction, which is perpendicular to its axis in z and the flow velocity in x.

Three gradually improved models of the VIVACE modulo were built and tested until the system was debugged. All data and results reported in Secs. 4 and 5 pertain to Model III. VIVACE Model III has $D=125.7$ mm, $L=914.4$ mm, and is made of aluminum. The aspect ratio of this cylinder is small at 7.274. The blockage ratio is 14.3% in the working section of the water channel. The cylinder is suspended by two compression coil-springs attached to the end-plates. The cylinder is constrained by linear bearings to vibrate freely in the y-direction. There were narrow gaps of about 10 mm between the walls of the water-channel and the end-plates of the model. The natural frequency $f_{n,\text{water}}$ of the oscillating cylinder system was controlled in the range of 0.88–1.037 Hz by adjusting the number of active coils in the coil-springs. The values of Reynolds number, UD/ν (ν =kinematic viscosity$=1.13899\times10^{-6}$ m^2/s for water at 15°C), used in the experiments are in the range of $\text{Re}=0.44-1.34\times10^5$.

End-plates. When a cylinder spans a wind/water tunnel, boundary effects may be significant, especially on the lift coefficient and the correlation length [39,40]. At higher Reynolds numbers, a reduction in the correlation of the neighboring zones and the instantaneous splitting of vortex shedding into cells each with a different shedding phase may occur [39,40]. Vortex shedding becomes irregular and affects the pressure fluctuations associated with vortex shedding [39–41]. It has been observed that the flow around a stationary cylinder for Reynolds number around 10^4 has a spanwise correlation of 3–4 diameters [40,41], which increases for an oscillating cylinder in VIV. The VIVACE Model III end-plates were designed to the size of the diameter of the cylinder to induce parallel shedding at high Reynolds number tests.

Figure 2 shows a picture of the VIVACE converter Model III with Parts 1–7 identified and listed in Table 1. The oscillating parts weights sum up to 16.79 kg, which includes one-third of the spring mass. The displaced fluid mass equals to 11.58 kg. This results in a ratio of oscillating mass over displaced fluid mass of 1.45.

2.3 Calibration. The vertical displacement $y(t)$ was measured using a Celesco cable extension position transducer (yo-yo potentiometer). The voltage measurement was done by directly connecting the generator to the data acquisition system. The data acquisition system from the position transducer and the generator consisted of a 16 bit analog to digital converter with four pole, low-pass, Butterworth filters. All data were collected at a 100 Hz sampling rate. The pressures are reported as an average over the steady-state portion of the time series. The record length was 30 s. for large amplitude oscillations.

Calibration of the LTFSW channel. Using a Pitot tube, velocity surveys were conducted to measure the velocity of the flow at different water depths of the tunnel. This produced a factor for various water depths which, when multiplied by the frequency of the impeller, determines the flow velocity. There is nonuniformity in the velocity of the flow as a function of the depth at velocities higher than 1.2 m/s [42]. This nonuniformity was not taken into account because all runs were conducted at velocities less than 1.2 m/s for which the variation along the depth was minimal. The Pitot tubes were positioned at 30 cm above the bottom of the tank and at half-width of the tank. Next, the velocity profiles were measured at one downstream location but at four other frequency settings on the drive motor at six different depths. The purpose of these profiles was to provide a calibration between the impeller frequency and the freestream velocity. The equation derived by correlation for the freestream velocity is U (m/s) $=(-0.000{,}034\times(\text{depth(mm)})+0.061{,}177)\times$ impeller frequency The correlation coefficient for the above linear equation between freestream velocity and the water depth is $R^2=0.994{,}211$. These values matched very well with the averaged value measured using

Table 1 Main components of the VIVACE Model III

Part No.	Description	No. of parts
1	5 in. cylinder	1
2	Rotat. generator	1
3	Gear	2
4	Side strut	2
5	Linear bearings	4
6	Fixed shafts	2

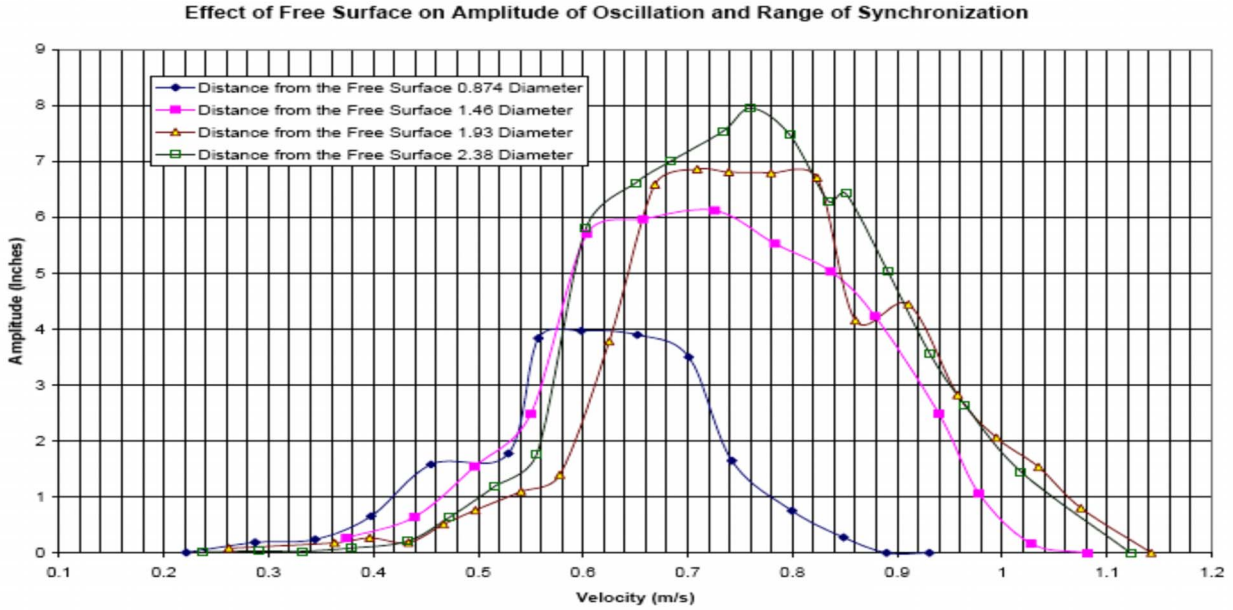

Fig. 3 Experimental results on the effect of free-surface on the amplitude of oscillation

the formula in Ref. [42].

Experimental assessment of the effect of free-surface. It is critical to know the effect of free-surface on the oscillation amplitude and on the range of synchronization of VIVACE. The effect of free-surface was studied by carrying a series of tests with the results compiled in Fig. 3. In these tests, the distance of the cylinder from the free-surface was varied. It is observed that free surface does affect the amplitude of vibration. As the cylinder gets closer to the free-surface, the amplitude of vibration and the range of synchronization are considerably reduced. Further verification is required by using a smaller diameter cylinder.

3 Mathematical Model

The mathematical model presented in Ref. [1] provided the following relations

(i) A simple equation of motion for the VIVACE cylinder in VIV:

$$(m^* + C_a)^* \left(\frac{\ddot{y}^*}{f_{n,\text{water}}^2} + \frac{4\pi\zeta_{\text{total}}\dot{y}^*}{f_{n,\text{water}}} + 4\pi^2 y^* \right) = \frac{2}{\pi} c_y(t) U^{*2} \tag{1}$$

whose dimensional form is

$$(m_{\text{osc}} + m_a)\ddot{y} + c_{\text{total}}\dot{y} + ky = \frac{2}{\pi D} c_y(t) m_d U^2 \tag{2}$$

$$y^* = y^*_{\text{max}} \sin(2\pi f_{\text{fluid}} t) \tag{3}$$

$$c_y(t) = C_y \sin(2\pi f_{\text{fluid}} t + \phi) \tag{4}$$

(ii) An expression for the fluid power in VIVACE:

$$P_{\text{VIVACE-fluid}} = \frac{1}{2}\rho\pi C_y U^2 f_{\text{cyl}} y_{\text{max}} DL \sin(\phi) \tag{5}$$

(iii) An expression for the mechanical power in VIVACE:

$$P_{\text{VIVACE-Mech}} = 8\pi^3 (m_{\text{osc}} + m_a)\zeta_{\text{total}} (y_{\text{max}} f_{\text{cyl}})^2 f_{n,\text{water}} \tag{6}$$

(iv) An equation relating mechanical to fluid particulars of a VIVACE cylinder in VIV derived directly from Eqs. (5) and (6) above:

$$C_y U^2 \sin(\phi) = 4\pi^3 D(m^* + C_a)\zeta_{\text{total}} y_{\text{max}} f_{\text{cyl}} f_{n,\text{water}} \tag{7}$$

where it was assumed that we can measure experimentally three of the four quantities C_y, $\sin(\phi)$, y_{max}, ζ_{total} and solve for the fourth.

(v) An upper limit to the power of the VIVACE converter based on experimentally measured data is:

$$\eta_{\text{UL-VIVACE}} = \frac{P_{\text{VIVACE-fluid}}}{\text{power in the fluid}} = \frac{\frac{1}{2}\rho\pi C_y U^2 f_{\text{cyl}} y_{\text{max}} DLs \text{ in } \phi}{\frac{1}{2}\rho U^3 DL} \tag{8}$$

(vi) An expression for the VIVACE converter based on experimentally measured power:

$$\eta_{\text{VIVACE}} = \frac{P_{\text{VIVACE-harn}}}{\text{power in the fluid}} = \frac{P_{\text{VIVACE-harn}}}{\frac{1}{2}\rho U^3 DL} \tag{9}$$

All symbols used in the above equations are defined in Table 2 in Ref. [1].

The purpose of the mathematical model developed below is to complement the above equations by modeling the transmission between the VIVACE cylinder and the generator, the generator, and the harnessed energy from the generator.

3.1 Generator Model. Consider the separately excited generator type depicted in Fig. 4 below.

Here E is the armature (induced) voltage, $\dot{\theta}$ is the radial veloc-

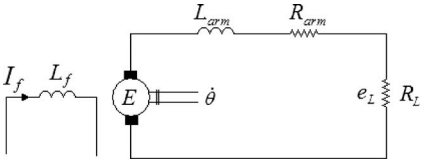

Fig. 4 Separately excited generator used for the mathematical model

ity of the generator shaft, L_{arm} is the armature inductance in henry, R_{arm} is the armature resistance in Ω, I_f is the field current, L_f is the field inductance, R_L is the external load resistance, and e_L is the voltage across the resistor R_L.

The torque T_{gen} of a generator is proportional to the armature current I_{arm} (by the constant K) and the air gap flux ψ, which is proportional to the field current by the constant k_f [32] as

$$\psi = k_f I_f \tag{10}$$

$$T_{gen} = (k_f I_f) \cdot (\bar{k} I_{arm}) \tag{11}$$

For the presented model, we consider a constant field current and assume that the geometric natural plane (GNP) and the magnetic natural plane (MNP) are coincident, yielding constant flux. Hence the torque is directly proportional to the armature current

$$T_{gen} = K I_{arm} \tag{12}$$

where K is the motor-torque constant.

Voltage proportional to the flux and the angular velocity of the rotor is induced on the rotating armature.

$$E = \alpha \frac{d\theta}{dt} \tag{13}$$

where α is the generator constant to relate the radial velocity of the generator shaft to the armature induced voltage. The armature current I_{arm} produces a torque T_{gen}, which balances the inertia and viscous forces of the rotor. Thus,

$$J \frac{d^2\theta}{dt^2} + c \frac{d\theta}{dt} = K I_{arm} \tag{14}$$

where J is the inertia of the rotor and c is the frictional losses coefficient. The external losses from gear and other mechanical parts attached will be added in Sec. 3.2 where the transmission model is introduced.

By the Kirchoff voltage law (see Fig. 4),

$$L_{arm} \frac{dI_{arm}}{dt} + R_{arm} I_{arm} + R_L I_{arm} = E \tag{15}$$

Let $\sim$ denote the amplitude of a complex variable. Let the transverse cylinder motion be the particular solution of the second order differential equation of forced motion of the cylinder, and let ω be the frequency of oscillation of the cylinder ω_{cyl}. Then,

$$y = \mathrm{Re}\{\tilde{y} e^{i\omega t}\} \tag{16}$$

the voltage across R_L is given by

$$\tilde{e}_L e^{i\omega t} \ldots \tag{17}$$

and the armature current is

$$\tilde{I}_{arm} e^{i\omega t} \tag{18}$$

Combining Eqs. (12)–(18) yields

$$\tilde{I}_{arm}\{L_{arm} i\omega + R_{arm}\} + \tilde{e}_L = i\omega\alpha\tilde{\theta} \tag{19}$$

and

$$\{(-\omega^2)J + \omega c\}\tilde{\theta} = K\tilde{I}_{arm} \tag{20}$$

Eliminating I_{arm} from the last two equations yields

$$\frac{\tilde{\theta}}{\tilde{e}_L} = \frac{-K}{i\omega\{-\omega^2 J L_{arm} + i\omega(L_{arm} c + R_{arm} J) + R_{arm} c - \alpha K\}} \tag{21}$$

3.2 Transmission Model. The linear oscillatory mechanical motion of the VIVACE cylinder in VIV is converted to a rotational oscillatory motion of the generator shaft via a gear system, as presented schematically in Fig. 5. We first consider though a

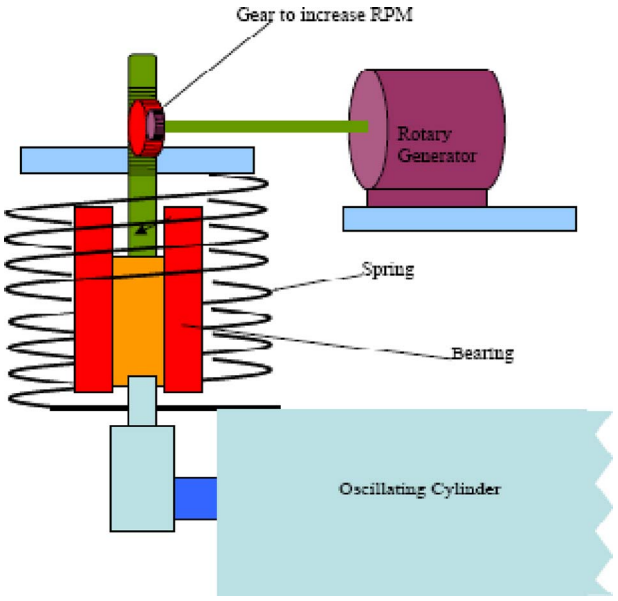

Fig. 5 VIVACE with a two-gear transmission system

generic transmission system between two shafts coupled through a two-gear system, as shown in Fig. 6. Assuming that both shafts are rigid and that there is no slip,

$$T_1 \dot{\theta}_1 = T_2 \dot{\theta}_2 \tag{22}$$

and

$$r_1 \dot{\theta}_1 = r_2 \dot{\theta}_2 \tag{23}$$

where n_i is the number of teeth, r_i is the radius, and T_i is the torque of the ith wheel. In the case where the number of teeth in a wheel is proportional to the radius of the wheel, we have

$$\frac{r_1}{r_2} = \frac{n_1}{n_2} = \frac{\dot{\theta}_2}{\dot{\theta}_1} \tag{24}$$

Let T_{gen} be the torque taken by the generator shaft, T_1 be the torque (supplied by Gear 2) on Gear 1, and let c_i denote the damping coefficient due to the frictional losses on the ith shaft. Then,

$$J_1 \frac{d^2\theta_1}{dt^2} + c_1 \frac{d\theta_1}{dt} = T_1 - T_{gen} \tag{25}$$

Let T_{viv} be the torque supplied to Shaft 2 induced by the linear motion of the cylinder in VIV, and T_2 be the torque transmitted to gear 2. Then,

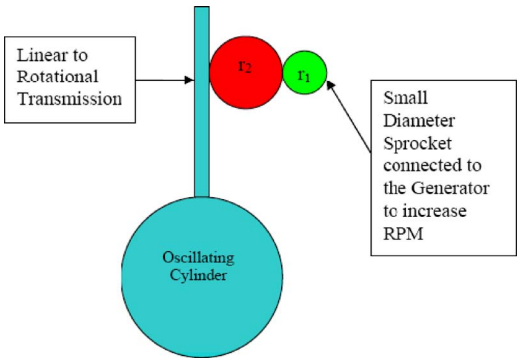

Fig. 6 Schematic of a two-shaft transmission system

$$J_2\frac{d^2\theta_2}{dt^2}+c_2\frac{d\theta_2}{dt}=T_{\text{viv}}-T_2 \tag{26}$$

Equations (22) and (23) yield

$$T_1=T_2\frac{\dot{\theta}_2}{\dot{\theta}_1}=T_2\frac{n_1}{n_2} \tag{27}$$

Due to Eqs. (26) and (27), Eq. (25) becomes

$$J_1\frac{d^2\theta_1}{dt^2}+c_1\frac{d\theta_1}{dt}+\frac{n_1}{n_2}\left(J_2\frac{d^2\theta_2}{dt^2}+c_2\frac{d\theta_2}{dt}-T_{\text{viv}}\right)=-T_{\text{gen}} \tag{28}$$

Since $\dot{\theta}_2=(n_1/n_2)\dot{\theta}_1$, we can rewrite Eq. (28) as

$$\left(J_1+\left(\frac{n_1}{n_2}\right)^2J_2\right)\frac{d^2\theta_1}{dt^2}+\left(c_1+\left(\frac{n_1}{n_2}\right)^2c_2\right)\frac{d\theta_1}{dt}-\frac{n_1}{n_2}T_{\text{viv}}=-T_{\text{gen}} \tag{29}$$

or

$$J_1^{\text{eq}}\frac{d^2\theta_1}{dt^2}+c_1^{\text{eq}}\frac{d\theta_1}{dt}=nT_{\text{viv}}-T_{\text{gen}} \tag{30}$$

where we define

$$J_1^{\text{eq}}\equiv\left(J_1+\left(\frac{n_1}{n_2}\right)^2J_2\right),\quad c_1^{\text{eq}}\equiv\left(c_1+\left(\frac{n_1}{n_2}\right)^2c_2\right),\quad n=\frac{n_1}{n_2}$$

In the same manner, for Gear 2, we have

$$J_2^{\text{eq}}\frac{d^2\theta_2}{dt^2}+c_2^{\text{eq}}\frac{d\theta_2}{dt}=T_{\text{viv}}-\frac{1}{n}T_{\text{gen}} \tag{31}$$

where

$$J_2^{\text{eq}}\equiv\left(J_2+\left(\frac{n_2}{n_1}\right)^2J_1\right),\quad c_2^{\text{eq}}\equiv\left(c_2+\left(\frac{n_2}{n_1}\right)^2c_1\right)$$

Based on Eq. (30), we can rewrite Eq. (21) as

$$\frac{\tilde{\theta}}{\tilde{e}_L}=\frac{-K}{i\omega\{-\omega^2J_1^{\text{eq}}L_{\text{arm}}+i\omega(L_{\text{arm}}c_1^{\text{eq}}+R_{\text{arm}}J_1^{\text{eq}})+R_{\text{arm}}c_1^{\text{eq}}-\alpha K\}} \tag{32}$$

3.3 Combined VIV, Transmission, Generator, Harnessed Energy Model. The force exerted on the cylinder rod by Gear 2 is due to the inertia of the generator, the friction forces in the generator, the inertia of the gear components, the friction forces in the gear components, and the electrical damping of the generator controlled by the load resistor R_L. Thus,

$$F_{\text{gear 2/cylinder}}=\frac{\Sigma M_{\text{gear 2}}}{r_2}=\frac{\left(J_1^{\text{eq}}\frac{d^2\theta_1}{dt^2}+c_1^{\text{eq}}\frac{d\theta_1}{dt}+KI_{\text{arm}}\right)\left(\frac{r_2}{r_1}\right)}{r_2} \tag{33}$$

Using Ohm's law and Eq. (32), we have

$$\tilde{I}_{\text{arm}}=\frac{1}{R_L}\frac{i\omega\{-\omega^2J_1^{\text{eq}}L_{\text{arm}}+i\omega(L_{\text{arm}}c_1^{\text{eq}}+R_{\text{arm}}J_1^{\text{eq}})+R_{\text{arm}}c_1^{\text{eq}}-\alpha K\}}{-K}\tilde{\theta}_1 \tag{34}$$

Substituting Eq. (34) into Eq. (33) yields

$$\tilde{F}_{\text{gear 2/cylinder}}=\left\{\begin{array}{c}\\ \\ -\omega^2J_1^{\text{eq}}+i\omega c_1^{\text{eq}}+\dfrac{i\omega\left\{\begin{array}{c}-\omega^2J_1^{\text{eq}}L_{\text{arm}}\\ +i\omega\left(\begin{array}{c}L_{\text{arm}}c_1^{\text{eq}}+\\ R_{\text{arm}}J_1^{\text{eq}}\end{array}\right)\\ +R_{\text{arm}}c_1^{\text{eq}}-\alpha K\end{array}\right\}}{R_L}\end{array}\right\}\frac{\tilde{\theta}_1}{r_1} \tag{35}$$

Combining Eq. (35) with the relation $\tilde{\theta}_1=\tilde{y}/r_1$ yields

$$\tilde{F}_{\text{gear 2/cylinder}}=\left\{\begin{array}{c}\\ \\ -\omega^2J_1^{\text{eq}}+i\omega c_1^{\text{eq}}+\dfrac{i\omega\left\{\begin{array}{c}-\omega^2J_1^{\text{eq}}L_{\text{arm}}\\ +i\omega\left(\begin{array}{c}L_{\text{arm}}c_1^{\text{eq}}\\ +R_{\text{arm}}J_1^{\text{eq}}\end{array}\right)\\ +R_{\text{arm}}c_1^{\text{eq}}-\alpha K\end{array}\right\}}{R_L}\end{array}\right\}\frac{\tilde{y}}{r_1^2} \tag{36}$$

where $\tilde{y}$ is the complex amplitude of the cylinder in VIV, as defined in Ref. [8]. As was assumed in Ref. [1], when the cylinder is in VIV, its motion $y(t)$ can be approximated by the following linear equation.

$$(m_{\text{osc}}+m_a)\ddot{y}+c_{\text{total}}\dot{y}+ky=\frac{2}{\pi D}c_y(t)m_dU^2 \tag{37}$$

Its dimensionless counterpart takes the form of Eq. (1) while the particulars of the forcing function on the right-hand side (RHS) are provided by Eqs. (3) and (4). Assuming that the system behaves linearly and responds at the frequency of excitation, Eq. (37) takes the following complex form

$$\tilde{y}\{-\omega^2(m_{\text{osc}}+m_a)+i\omega c_{\text{total}}+k\}=\tilde{F} \tag{38}$$

where c_{total} is the sum of all damping coefficients as described in detail in Sec. 3.5).. The forces on the cylinder rod are due to VIV (exiting force) and the generator via the gear transmission (damping+inertia forces)

$$\tilde{F}=\tilde{F}_{\text{viv/cylinder}}-\tilde{F}_{\text{generator/cylinder}} \tag{39}$$

Combining Eqs. (37)–(39) yields Eq. (40)

$$\begin{aligned}&\tilde{y}\{-\omega^2(m_{\text{osc}}+m_a)+i\omega c_{\text{system}}+k\}\\&\quad=-\left\{-\omega^2J_1^{\text{eq}}+i\omega c_1^{\text{eq}}+\frac{i\omega\{-\omega^2J_1^{\text{eq}}L_{\text{arm}}+i\omega(L_{\text{arm}}c_1^{\text{eq}}+R_{\text{arm}}J_1^{\text{eq}})+R_{\text{arm}}c_1^{\text{eq}}-\alpha K\}}{R_L}\right\}\frac{\tilde{y}}{r_1^2}+\tilde{F}_{\text{viv/cylinder}}\end{aligned} \tag{40}$$

where c_{system} describes the damping of the oscillating cylinder without the gear system and the generator. The damping of the gear system, the frictional losses of the rotating shaft of the generator, the power losses across the inner resistance R_{arm}, and the harnessed damped power across load resistor R_L are described in the RHS of Eq. (40) (this is explained in detail in Sec. 3.5). Collecting terms by $\tilde{y}$ in Eq. (40) yields the relation between the amplitude of oscillation, the VIV forces, the inertia and friction terms of all rotating and moving parts, and the electrical load (harnessed and dissipated),

$$\tilde{y} = \frac{\tilde{F}_{\text{viv/cylinder}}}{\{-\omega^2(m_{\text{osc}} + m_a) + i\omega c_{\text{system}} + k\} + \left\{-\omega^2 J_1^{\text{eq}} + i\omega c_1^{\text{eq}} + \frac{i\omega\{-\omega^2 J_1^{\text{eq}} L_{\text{arm}} + i\omega(L_{\text{arm}} c_1^{\text{eq}} + R_{\text{arm}} J_1^{\text{eq}}) + R_{\text{arm}} c_1^{\text{eq}} - \alpha K\}}{R_L}\right\} \frac{1}{r_1^2}} \tag{41}$$

with

$$J_1^{\text{eq}} \equiv \left(J_1 + \left(\frac{n_1}{n_2}\right)^2 J_2\right)$$

$$c_1^{\text{eq}} \equiv \left(c_1 + \left(\frac{n_1}{n_2}\right)^2 c_2\right)$$

3.4 Damping. A very important variable is the total damping coefficient

$$c_{\text{total}} = c_{\text{system}} + c_{\text{tra}} + c_{\text{gen}} + c_{\text{harn}} \tag{42}$$

as defined in Ref. [1]. An analytical estimation of c_{total} for a VIVACE cylinder in VIV is not possible. Consequently, damping is measured experimentally and the results for VIVACE Model III are provided in Chap. 4.

For a VIVACE cylinder in VIV, there are four sources of damping, as shown in Eq. (42). The system damping c_{system} includes structural damping and fluid damping. The former is caused by friction at the component and the material scales. It is measured by performing a damping test in air (ideally in vacuum). The fluid damping is the result of energy dissipation as the fluid moves relative to the vibrating structure. The transmission damping c_{tra} is due to friction in the gear system and frictional losses of the generator as frictional bearing losses. The generator damping c_{gen} is due to the generator armature (internal) resistance R_{arm} (magnetic losses are neglected at this stage for the linear mathematical model). Finally, c_{harn} is the damping due to the load resistance R_L used to harness energy. The following damping tests are conducted to assess the quality of the VIVACE model, and some of the measurements can be used to calculate the components of Eq. (42).

(i) In air with gear disconnected: It provides data to calculate the component of c_{system} due to structural damping.
(ii) In water with gear disconnected: It provides data to calculate the sum of c_{system} due to structural damping plus damping due to stationary fluid.
(iii) In water with transmission connected and generator connected to the transmission (without electrical load): It provides data to calculate the sum of the c_{system} part due to structural damping, plus fluid damping due to the cylinder motion in stationary fluid, plus frictional losses due to the gear transmission and generator. This provides data to calculate c_{tra}.

The generator damping c_{gen} (due to the generator armature internal resistance R_{arm}) is a function of the load resistance. For the open circuit case where the load resistance goes to infinity, the electrical losses due to the inner resistance are zero. The inner power losses are calculated by $(e_L/R_L)^2 R_L$, where e_L is the measured voltage on the load resistor R_L. After all damping tests, the harnessed power is measured and compared to the calculated power, as explained in Sec. 4.5 and Chap. 5.

The above damping coefficients (except of course for the electrical damping coefficients c_{gen} and c_{harn}) are calculated by performing a free decay test of the corresponding system. An initial displacement is given to the structure (cylinder), resulting in a damped oscillation of the structure. If y_n and y_{n+1} are two consecutive peaks of a linear system, we have

$$\frac{y_n}{y_{n+1}} = \frac{A_y \exp(-\zeta\omega_d t)}{A_y \exp(-\zeta\omega_d (t + T_d))} = \exp(\zeta\omega_d T_d) \tag{43}$$

where T_d is the period of the oscillation $T_d = 2\pi/\omega_d$. Hence the damping ratio ζ is

$$\zeta = \frac{1}{2\pi} \ln \frac{y_n}{y_{n+1}} \tag{44}$$

where y_n and y_{n+1} are measured experimentally.

3.5 Measured Power. VIVACE Model III engages only one gear of radius r_1 and is, thus, simpler than the system depicted in Figs. 5 and 6. The open circuit voltage coefficient of the generator relating the radial velocity of the generator to the open circuit voltage, as provided by Eq. (13), is $\alpha = 0.4297$. For a given vertical velocity of the cylinder and with no relative slip between the belt and gear, the radial velocity of the generator as a function of the vertical velocity of the cylinder is

$$\dot{\theta} = \frac{\dot{y}}{r_1} \tag{45}$$

where r_1 is the radius of the gear and equals 0.013,617 m. The armature (inner) resistance of the generator R_{arm} equals 7 Ω. The open voltage of the generator is

$$E = \alpha\dot{\theta} = \alpha\frac{\dot{y}}{r_1} \tag{46}$$

Hence, the power harnessed (P_L) by the load resistor R_L can be estimated for the simple case by

$$P_L = e_L I_{\text{arm}} = {I_{\text{arm}}}^2 R_L = \left(\frac{\frac{\dot{y}(t)}{r_1}\alpha}{R_{\text{arm}} + R_L}\right)^2 R_L \tag{47}$$

Based on this equation and on the measured displacement time record and calculated velocity, the harnessed power can be calculated and compared to the measured and power time record. This is shown in Chap. 4.

4 Measurements and Data Analysis

Using the LTFSW channel and the VIVACE Model III described in Chap. 2, the following quantities were recorded in each run:

(i) the cylinder vertical displacement $y(t)$
(ii) the water velocity U
(iii) the voltage generated at the load resistance R_L used to harness electricity
(iv) the harnessed power $P(t)$.

In this chapter, sample damping test results, the method of data analysis, and the verification of accuracy and compatibility of measurements are presented.

4.1 Damping Tests. Several damping tests were conducted to evaluate the design, fabrication, and mounting of the various VIVACE models built and tested over a period of about 5 months. A few sample results presented here are from the measurements conducted on VIVACE Model III. The purpose of all damping tests was to make sure that friction was low and all components

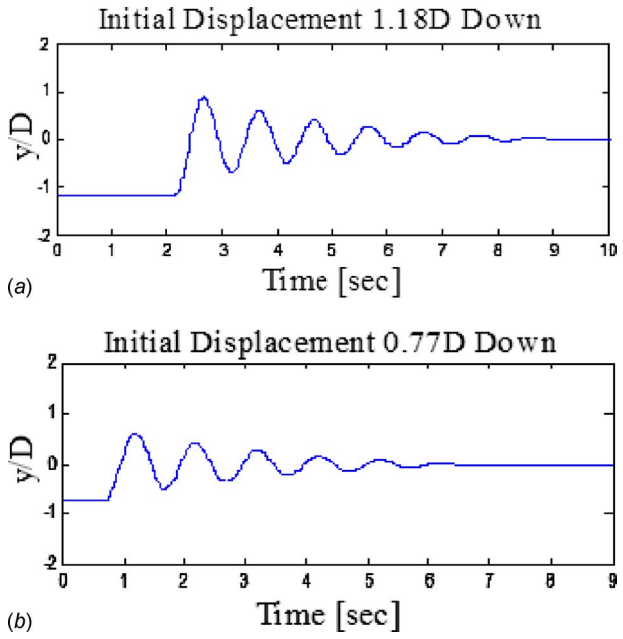

Fig. 7 Typical recorded time histories of free decay oscillation in water for VIVACE Model III with gear disconnected

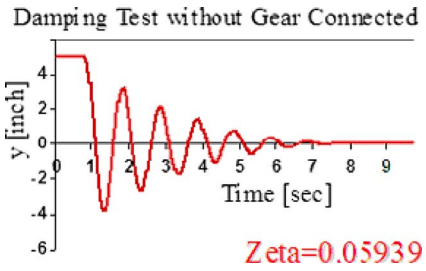

Fig. 9 Free decay damping test in water for VIVACE Model III with disconnected transmission

were functioning and were properly aligned. Damping tests (see Fig. 7) were conducted on a regular basis every few hours of model tests and included the tests specified in Sec. 3.5. As explained in Chap. 2, special attention was paid to free-surface and bottom effects.

Figure 8 shows two samples from a series of tests conducted in water with gear disconnected. The calculated damping factor corresponds to ζ_{system} for different initial displacement values. The results are plotted in Fig. 9 and compare very well to damping test results for similar apparatus, as compiled by Sumer and Fredsoe [17].

Figures 9–11 show a sequence of damping tests in still water with additional components connected progressively. The test results reveal that there is a significant amount of energy that can be harnessed and a lot that is dissipated in various forms of loss. Results also imply that there is room for improvement in the model.

4.2 Data Analysis. The time series recorded from test runs were analyzed using the Hilbert–Huang transform (HHT). This transform was selected because of the nonlinear and nonstationary nature of the VIV time series. Fourier spectral analysis can only be applied to linear, periodic, and stationary time series [43].

Fourier spectral analysis decomposes a time series $f(t)$ into global sinusoidal components of fixed amplitude a_j.

$$f(t) = \sum_{j=0}^{n} a_j e^{i\omega_j t} \tag{48}$$

$$a_j = \frac{1}{2\pi}\int_t f(t)e^{-i\omega_j t}dt \tag{49}$$

The spectrals amplitude a_j yield the energy contributed by a sinusoid at frequency ω_j that spans the whole time series. This decomposition makes sense with the underlying process. If the data is not a pure sinusoidal, the Fourier spectral analysis will contain harmonics. The time series recomposed in form (48) would be stationary, since the a_j are constant.

HHT has been proposed by Huang et al. [43] for nonstationary and nonlinear time series analysis. The software is commercially available and it has been patented by NASA. This method has gained much popularity and has been explored for its use in vari-

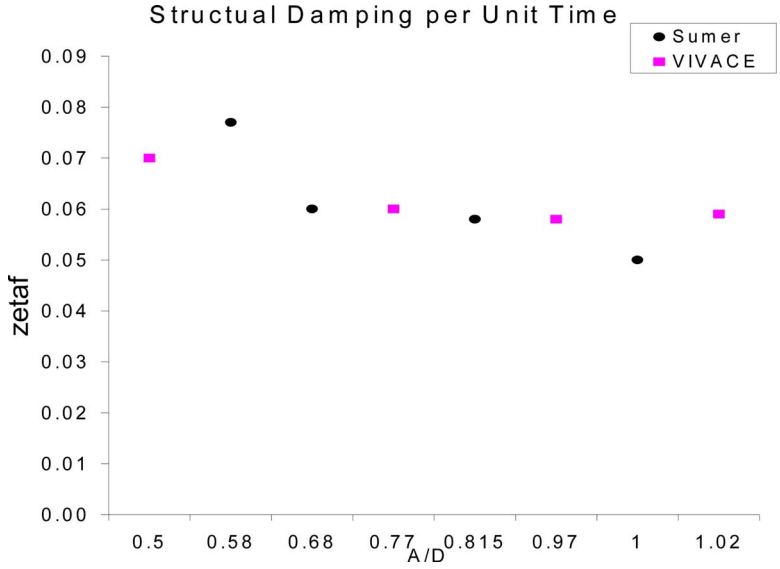

Fig. 8 Free decay damping test results in water: comparison between VIVACE Model III with gear disconnected and Sumer's compiled data [36]

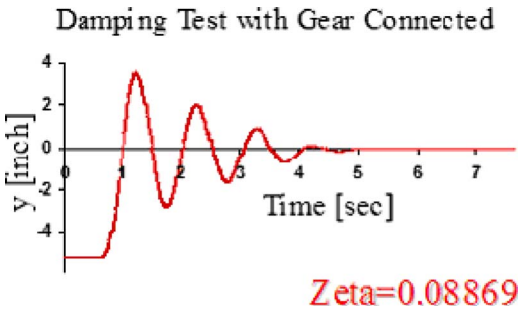

Fig. 10 Free decay damping test in water for VIVACE Model III with connected transmission but disconnected generator

ous fields such as medical imaging, acoustic vibration, seismic analysis, nonlinear water wave analysis [44], and VIV analysis [45]. The Hilbert transform has been a popular method for estimating natural frequency and damping ratio for various nonlinear signals [15]. This method provides good results if the nonlinear signal being analyzed contains one predominant frequency. For a signal containing several frequencies, it provides confusing results [43]. Empirical mode decomposition (EMD) proposed by Huang can be used to separate different frequency components called intrinsic mode functions (IMFs). An IMF is a function, which satisfies two conditions [43] (a) "In the whole data set, the number of extrema and the number of zeros crossings must either be equal or differ at most by one," and (b) "At any point, the mean value of the envelope defined by the local maxima and the envelope defined by the local minima is zero." Then, the method of Hilbert transform can be used to estimate the instantaneous frequencies of IMFs. The instantaneous frequencies, being functions of time, identify imbedded phenomena, which a Fourier analysis cannot reveal. IMFs provide a physical sense of the phenomena. By using HHT, we can examine the detailed dynamic characteristics of a nonlinear system through its instantaneous frequency and IMFs.

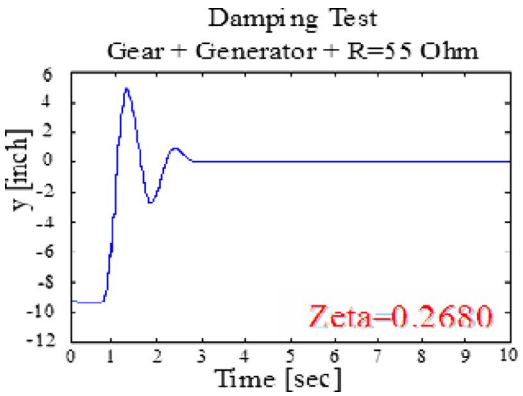

Fig. 11 Free decay damping test in water for VIVACE Model III with connected transmission, generator, and R_L=55 Ω.

4.3 Measured Power. Several tests were conducted spanning a broad range of velocities and energy harnessing resistors R_{load}. The resistor voltage was measured along with the harnessed power. The results are presented in Chap. 5. In this section, an example is shown to verify consistency of measurements based on Eq. (47) derived in Chap. 3.

In the case considered here, the test velocity was U =0.840 m/s=1.63 kn, the load resistor was R_L=80 Ω (see Figs. 14–16). This resulted in the highest measured efficiency, as shown in Chap. 5. This case was also used in Chap. 4 of Ref. [7] in benchmarking. The maximum peak efficiency achieved for the tested VIVACE modulo is

$$\eta_{peak} = 0.308 \tag{50}$$

The corresponding integrated power efficiency in that particular test is approximately

$$\eta_{VIVACE} = 0.22 \tag{51}$$

The theoretical upper limit based on measurements is

$$\eta_{UL\text{-}VIVACE} = 0.3663 \tag{52}$$

Figure 12 shows 60 s of recorded signals for R_L=80 Ω and U =0.805 m/s. The measured cylinder displacement $y(t)$, the voltage at the load resistor ends $V_{load}(t)$, and power; and calculated cylinder velocity $\dot{y}(t)$ are shown in Fig. 12. The cylinder velocity is calculated by time differentiation of the cylinder displacement.

The calculated power $P(t)$ using Eq. (47) is based on the following values.

(i) The open circuit voltage coefficient of the generator relating the radial velocity of the generator to the open circuit voltage is α=0.4297.
(ii) The radius of the gear wheel is r=0.013617 m.
(iii) The armature (inner) resistance of the generator is R_{arm} =7.0 Ω.

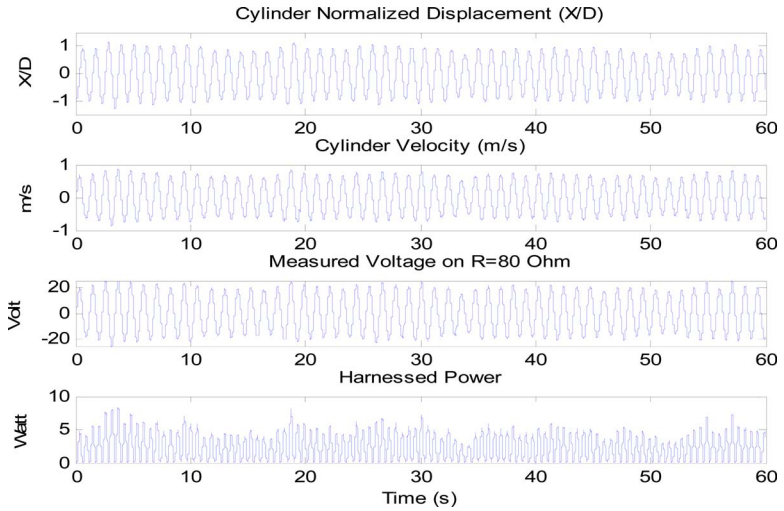

Fig. 12 Time histories of measured cylinder displacement, potential, and power; and calculated cylinder velocity

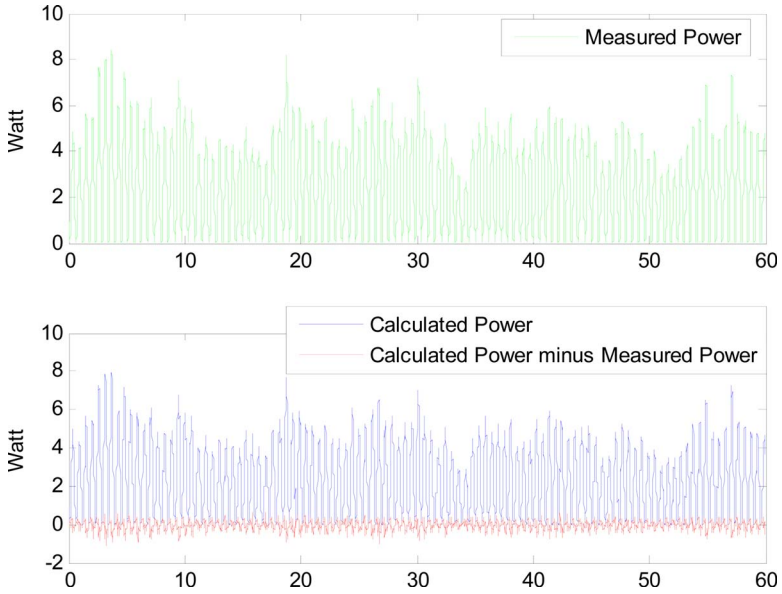

Fig. 13 Comparison of measured harnessed power to the power calculated using Eq. (47)

The compatibility of the results in Fig. 12 provides a verification that the measurements of cylinder displacement, potential, power, and generator and transmission particulars are quite accurate (see Fig. 13) [46].

5 Test Results

Figures 14 and 15 show the measured dimensionless amplitude of VIV and the measured power output, respectively. Figure 16 shows the efficiency calculated using Eq. (9). We can make several observations based on these results.

(a) Figure 14 shows that as R_L increases—that is damping decreases per Eqs. (41) and (47)—the VIV amplitude and range of synchronization increase.
(b) For R_L of infinity, the electrical power takeoff goes to zero as the generator ends are open and current is zero.
(c) Figure 14 shows that the amplitude of oscillation and range of synchronization remain high even at the high damping values used. This is necessary for extracting generating energy using VIV.
(d) Figure 16 shows that the maximum peak efficiency reaches a value of 30.77% corresponding to an integrated efficiency in a cycle of 22% and an upper limit of 36.63%. This is achieved by approximately optimizing the system with respect only to one variable R_L and even at the low speed of 0.840 m/s.
(e) It appears that the relatively high Reynolds number at which the experiments are conducted supports higher amplitudes of oscillation than those typically reported in the literature.

As a closing thought, it is worth comparing the VIVACE converter to a conventional engine such as a diesel. For a classical diesel-generator system, the rpm is only slightly affected by the power takeoff as long as the system is within the nominal values of the power takeoff as a function of the diesel specifications. That is, as long as we do not attempt to generate more energy than the diesel can supply for a given rpm, the diesel rpm is not affected by the power takeoff. In the case of VIVACE, higher damping (lower R_L) results in reduced motion and range of synchronization. If damping is increased too much, in an effort to extract more energy, VIV may be altogether suppressed. In other words, in this natural way of extracting energy from this renewable source there appears to be a natural self-limiting upper bound.

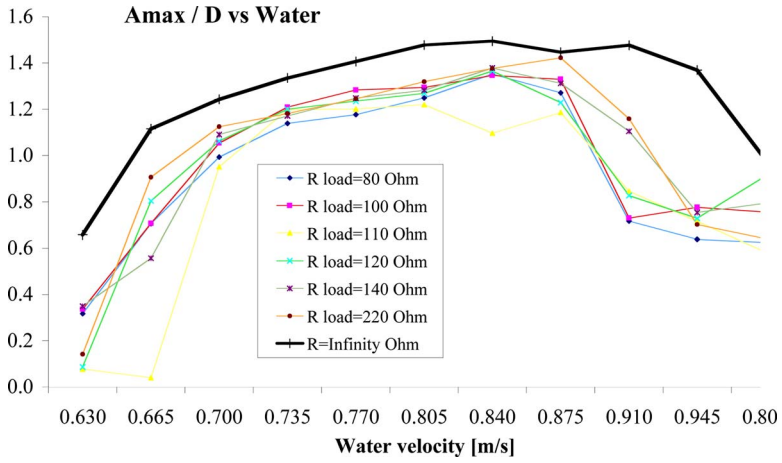

Fig. 14 Normalized amplitude versus water velocity for different R_L

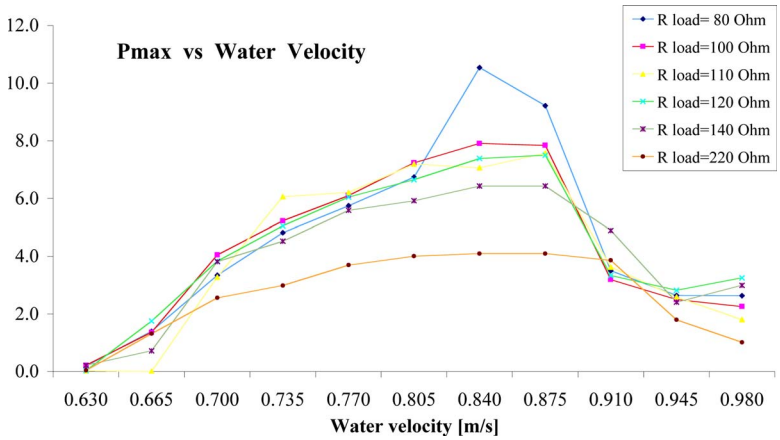

Fig. 15 Generated power versus water velocity for different R_L

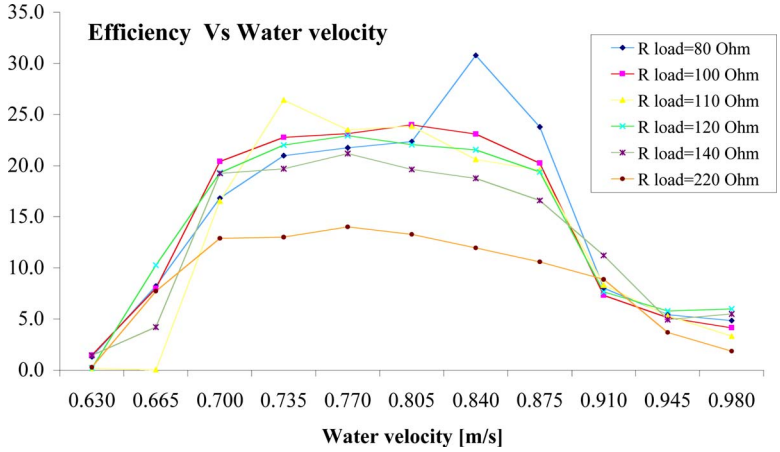

Fig. 16 Peak efficiency versus water velocity for different R_L

6 Conclusions

A single modulo of the VIVACE converter consisting of a circular cylinder mounted on elastic springs was tested in the Low Turbulence Free-Surface Water Channel of the Marine Hydrodynamics Laboratory of the University of Michigan. The following are the contributions of this paper.

(i) Even though numerous experiments have been conducted in VIV since the early 1900s, the regime of applicability to the design of the VIVACE converter had not been tested before. Specifically, for VIVACE to convert kinetic fluid flow energy to electricity, VIV has to be maintained under high damping [4,47].
(ii) In a realistic ocean environment, Reynolds number is high for energy generation, which proved to be beneficial as the amplitude of VIV increases significantly for high Re, a regime scarcely tested before.
(iii) A mathematical model was developed combining VIV with transmission via a gear-belt mechanism, a generator, and an energy harnessing electrical resistance. This model is compatible with the hydrodynamic model developed in our previous paper [1,4].
(iv) The mathematical model proved that measurements were consistent and accurate by comparing the measured harnessed power to the power calculated using data also collected during a particular test.
(v) The maximum peak efficiency achieved for the tested VIVACE modulo was $\eta_{peak}=0.308$. The corresponding integrated power efficiency in that particular test was $\eta_{VIVACE}=0.22$ with a theoretical upper limit based on the measurements of $\eta_{UL\text{-}VIVACE}=0.3663$. The test velocity was $U=0.840$ m/s=1.63 kn.
(vi) The results show that the VIVACE converter can convert kinetic energy to electricity with high efficiency even at low speeds where watermills and turbines cannot operate efficiently.

Future developments of the VIVACE converter include the following:

(a) conducting model tests with visualization to investigate the impact of high damping and high Reynolds number on wake mode
(b) investigating the impact of wake mode on energy extraction, which requires maintaining high amplitude VIV over a broad range of synchronization
(c) building the next generation of VIVACE models with smaller diameters, which will result in higher aspect ratios, allow for higher velocities at the same Reynolds number, and higher amplitudes of oscillation given the depth limitations of the testing facility
(d) optimizing the harnessed energy for a given m^*, by varying not only the electrical load resistance R_L but the spring stiffness k as well.

Acknowledgment

This research and development project has been supported by DOE Invention and Innovations Program Grant No. DE-FG36-

05GO15162 to Vortex Hydro Energy, ONR Grant No. N00014-03-1-0983 to the University of Michigan, and by the University of Michigan Grant Nos. U013752/U014243.

References

[1] Bernitsas, M. M., Ben-Simon, Y., Raghavan, K., and Garcia, E. M. H., 2008, "VIVACE (Vortex Induced Vibration Aquatic Clean Energy): A New Concept in Generation of Clean and Renewable Energy From Fluid Flow," ASME J. Offshore Mech. Arct. Eng., **130**(4), p. 041101

[2] Pontes, M. T., and Falcão, A., 2001, "Ocean Energies: Resources and Utilization," *Proceedings of 18th World Energy Council Congress*, Buenos Aires, Oct.

[3] WEC (World Energy Council, 2001), "Survey of Energy Resources," 19th ed., London, UK.

[4] Bernitsas, M. M., and Raghavan, K., 2004, "Converter of Current/Tide/Wave Energy," Provisional Patent Application, U.S. Patent and Trademark Office Serial No. 60/628,252.

[5] Bernitsas, M. M., and Raghavan, K., 2005, "Supplement to the U.S. Provisional Patent Application titled 'Converter Of Current, Tide, or Wave Energy'," University of Michigan Ref. No. 2973.

[6] Bernitsas, M. M., and Raghavan, K., 2005, "Fluid Motion Energy Converter," U.S. Patent Application, U.S. Patent and Trademark Office Serial No. 11/272,504.

[7] Bernitsas, M. M., and Raghavan, K., 2005, "Fluid Motion Energy Converter," International. Provisional Patent Application, USA Patent and Trademark Office.

[8] Clark, R. O., 1999, "Fluid Energy Converting Method and Apparatus" U.S. Patent and Trademark Office Patent No 4,347,036.

[9] Yoshitake, Y., Sueoka, A., Yamasaki, M., Sugimura, Y., and Ohishi, T., 2004, "Quenching of Vortex-Induced Vibrations of Towering Structure and Generation of Electricity Using Hula-Hoops," J. Sound Vib., **272**, pp. 21–38.

[10] Bearman, P. W., 1984, "Vortex Shedding From Oscillating Bluff Bodies," Annu. Rev. Fluid Mech., **16**, pp. 195–222.

[11] Carberry, J., Sheridan, J., and Rockwell, D., 2003, "Controlled Oscillations of a Cylinder: Forces and Wake Modes," J. Fluids Struct., **17**(2), pp. 337–343.

[12] Chen, S. S., 1987, *Flow-Induced Vibration of Circular Cylinder Structures*, Hemisphere Publishing, Springer, Washington.

[13] Blevins, R. D., 1990, *Flow-Induced Vibration*, 2nd ed., Van Nostrand Reinhold, New York.

[14] Griffin, O. M., and Koopmann, G. H., 1977, "The Vortex-Exited Lift and Reaction Forces on Resonantly Vibrating Cylinders," J. Sound Vib., **54**, pp. 435–448.

[15] Feldman, M., 1994, "Nonlinear System Vibration Analysis Using Hilbert Transform" Mech. Syst. Signal Process., **8**, pp. 119–127.

[16] Sarpkaya, T., 2004, "A Critical Review of the Intrinsic Nature of Vortex Induced Vibrations," J. Fluid Mech., **19**(4), pp. 389–447.

[17] Sumer, B. M., and Fredsoe, J., 1997, *Hydrodynamics Around Cylindrical Structures*, World Scientific, Singapore.

[18] Williamson, C. H. K., and Govardhan, R., 2004, "Vortex Induced Vibrations," Annu. Rev. Fluid Mech., **36**, pp. 413–455.

[19] Krishnamoorthy, S., Price, S. J., and Paidoussis, M. P., 2001, "Cross-Flow Past an Oscillating Circular Cylinder: Synchronization Phenomena in the Near Wake," J. Fluids Struct., **15**, pp. 955–980.

[20] Lu, X.-Y., and Dalton, C., 1996, "Calculation of the Timing of Vortex Formation From an Oscillating Cylinder," J. Fluids Struct., **10**(5), pp. 527–541.

[21] Williamson, C. H. K., 1996, "Vortex Dynamics in the Cylinder Wake," Annu. Rev. Fluid Mech., **28**, pp. 477–539.

[22] Carberry, J., 2002, "Wake States of a Submerged Oscillating Cylinder and of a Cylinder Beneath a Free-Surface," Ph.D. thesis, Monash University, Melbourne, Australia.

[23] Govardhan, R., and Williamson, C. H. K., 2000, "Modes of Vortex Formation and Frequency Response of a Freely Vibrating Cylinder," J. Fluid Mech., **420**, pp. 85–130.

[24] Khalak, A., and Williamson, C. H. K., 1996, "Dynamics of a Hydroelastic Cylinder With Very Low Mass and Damping," J. Fluids Struct., **10**(5), pp. 455–472.

[25] Khalak, A., and Williamson, C. H. K., 1999, "Motions, Forces and Mode Transitions in Vortex-Induced Vibrations at Low Mass-Damping," J. Fluids Struct., **13**, pp. 813–851.

[26] Willden, R. H. J., Kendon, T. E., and Graham, J. M. R., 2005, "Aspects of the Transverse Vortex-Induced Vibrations of Low Mass Ratio Elastically Supported Circular Cylinders," *Conference on Bluff Body Wakes and Vortex-Induced Vibrations (BBVIV4)*, Greece Jun. 21–24.

[27] Govardhan, R., and Williamson, C. H. K., 2005, "Revealing the Effect of Reynolds Number on Vortex-Induced Vibrations Using Controlled Negative and Positive Damping," *Conference on Bluff Body Wakes and Vortex-Induced Vibrations (BBVIV4)*, Greece, Jun. 21–24.

[28] Ding, J., Balasubramanian, S., Lokken, R., and Yung, T., 2004, "Lift and Damping Characteristics of Bare and Straked Cylinders at Riser Scale Reynolds Numbers," *Proceedings of Offshore Technology Conference*, Houston, TX, Paper No. 16341.

[29] Moe, G., Holden, K., and Yttervoll, P. O., 1994, "Motion of Spring Supported Cylinders in Subcritical and Critical Water Flows," *Proceedings of the Fourth International Offshore and Polar Engineering Conference*, Vol. 3, Osaka, Japan, June, pp. 468–475.

[30] Vikestad, K., 1998, "Multi-Frequency Response of a Cylinder Subjected to Vortex Shedding and Support Motions," Ph.D. thesis, Norwegian University of Science and Technology, Trondheim.

[31] West, G. S., and Apelt, C. J., 1982, "The Effects of Tunnel Blockage and Aspect Ratio on the Mean Flow Past a Circular Cylinder With Reynolds Numbers Between 10^4 and 10^5," J. Fluid Mech., **114**, pp. 361–377.

[32] Zhu, Q., Lin, J. C., Unal, M. F., and Rockwell, D., 2000, "Motion of a Cylinder Adjacent to a Free-Surface: Flow Patterns and Loading," Exp. Fluids, **28**, pp. 559–575.

[33] Bearman, P. W., and Zdravkovich, M. M., 1978, "Flow Around a Circular Cylinder Near a Plane Boundary," J. Fluid Mech., **89**, pp. 33–48.

[34] Miyata, H., Shikazono, N., and Kanai, M., 1990, "Forces on a Circular Cylinder Advancing Steadily Beneath the Free Surface," Ocean Eng., **17**, pp. 81–104.

[35] Gharib, M., and Weigand, A., 1996, "Experimental Studies of Vortex Disconnection and Connection at a Free Surface," J. Fluid Mech., **321**, pp. 59–86.

[36] Rood, E. P., 1995, "Free Surface Vorticity," *In Free-Surface Vorticity*, S. Green, ed., Kluwer, Norwell, Chap. 17.

[37] Sheridan, J., Lin, J. C., and Rockwell, D., 1997, "Flow Past a Cylinder Close to a Free Surface," J. Fluid Mech., **330**, pp. 1–30.

[38] Walker, D. T., Lyzenga, D. R., Ericson, E. A., and Lund, D., E., 1996, "Radar Backscatter and Surface Roughness Measurements for Stationary Breaking Waves," Proc. R. Soc. London, Ser. A, **452**, pp. 1953–1984.

[39] Norberg, C., 2003, "Fluctuating Lift on a Circular Cylinder: Review and New Measurements," J. Fluids Struct., **17**, pp. 57–96.

[40] Szepessy, S., and Bearman, P. W., 1992, "Aspect Ratio and End Plate Effects on Vortex Shedding From a Circular Cylinder," J. Fluid Mech., **234**, pp. 191–218.

[41] Szepessy, S., 1993, "On the Control of Circular Cylinder Flow by End Plates," Eur. J. Mech. B/Fluids, **12**, pp. 217–244.

[42] Maki, K. J., 2005, "Transom Stern Hydrodynamics" Ph.D thesis, University of Michigan, Ann Arbor.

[43] Huang, Norden E., Shen, Z., Long, S. R., Wu, M. C., Shih, E. H., Zheng, Q., Tung, C. C., and Liu, H. H., 1998, "The Empirical Mode Decomposition and the Hilbert Spectrum for Nonlinear and Nonstationary Time Series Analysis," Proc. R. Soc. London, Ser. A, **454**, pp. 903–995.

[44] Huang, N. E., Shen, Z., and Long, S. R., 1999, "A New View of Nonlinear Water Waves: The Hilbert Spectrum," Annu. Rev. Fluid Mech., **31**, pp. 417–457.

[45] Gharib, Mohammad Reza, 1999, "Vortex-Induced Vibration, Absence of Lock-In and Fluid Force Deduction," Ph.D. thesis, California Institute of Technology, Pasadena.

[46] Ben Simon, Y., 2005, "Highly Damped Vortex Induced Vibrations of Circular Cylinder" P.E. thesis, University of Michigan, Ann Arbor.

[47] U.S. Patent and Trademark Office http://www.uspto.gov/